

Electron density measurements and calculations in a helium capacitively-coupled radio-frequency plasma

¹Brian Z. Bentz, ²Peter Hartmann, ²Aranka Derzsi, ¹Kevin Youngman, ²Zoltán Donkó

¹ Sandia National Laboratories, 1515 Eubank Boulevard, Albuquerque, New Mexico, USA

² Institute for Solid State Physics and Optics, HUN-REN Wigner Research Centre for Physics, 1121 Budapest, Konkoly Thege Miklós str. 29-33, Hungary

E-mail: bzbentz@sandia.gov, donko.zoltan@wigner.hu

Abstract. We report a comparison of inferred electron density (n_e) in a He capacitively-coupled plasma, deduced from Laser-Collision Induced Fluorescence measurements, with values computed using a hybrid simulation framework based on Particle-in-Cell / Monte Carlo Collisions simulations and a fluid model for excited He atoms. The studies were carried out for gas pressures between 50 mTorr and 1000 mTorr and peak-to-peak radio-frequency (13.56 MHz) voltages between 150 V and 350 V, in a highly symmetric source equipped with plane-parallel electrodes. A good agreement is found between the experimental and modeling results for n_e except at the lowest operating voltages and gas pressures. The (effective) electron temperature (T_e) values derived by the two methods agree as well reasonably within the plasma bulk. The simulation results are used to compare the density distributions of He^+ and various He excited levels and their major populating and de-populating channels at 100 mTorr and 1000 mTorr.

Submitted to: *Plasma Sources Sci. Technol.*

1. Introduction

Capacitively-coupled radio-frequency discharges have been established as a key technology in the semiconductor industry for applications including plasma etching, sputtering, deposition, and cleaning [1–3]. However, fundamentals of their operation, including power absorption mechanisms, ionization dynamics, and plasma surface interactions, are not well understood [4–6]. While insights can be gained through experiments, it is difficult or impossible to measure all the parameters of interest. Therefore, simulations are also required for fundamental understanding and to investigate conditions not explored experimentally. Once validated, simulations can be used for plasma source design and to save time and costs that would otherwise be used to perform experimental testing.

The electron density (n_e) is perhaps the most attractive parameter to measure for validation of plasma simulations because the distributions of charged species and neutrals in the plasma are (mostly) determined by electron-impact collisions. However, a precise measurement of n_e is challenging. Electrical probes are commonly used, including Langmuir probes [7], hairpin probes [8], cutoff probes [9], and multipole resonance probes [10]. For example, a floating hairpin resonator probe was used in [11] to measure electron density within the radio-frequency cycle of a parallel plate capacitively-coupled plasma. In this work, a time resolution capable of detecting electron density oscillations within the radio-frequency cycle was demonstrated. A multipole resonance probe was used in [12] to measure electron density in a large area capacitively-coupled plasma driven by multiple frequencies. Translating the probe provided spatial resolutions of a few centimeters, revealing density gradients for different relative phase shifts influencing the self-bias voltage. As demonstrated in these examples, the probe theories and data evaluation methods must be used very carefully as a function of the actual conditions to obtain meaningful results. Furthermore, electrical probes are known to be invasive, and they alter the plasma density due to their very presence. Alternative measurement approaches are also desirable.

As non-intrusive alternatives to the probe methods, microwave interferometry [13] and laser diagnostics methods [14] may be considered. Among the latter, Thomson scattering [15] and Laser-Collision Induced Fluorescence (LCIF) [16, 17] measurements have proven particularly useful. For example, Thomson scattering was used in [18] to observe the electron energy distribution function in a capacitively-coupled RF argon plasma. The distribution function was found to change from a bi-Maxwellian at 100 mTorr to a single Maxwellian at 500 mTorr, confirming probe measurements made in similar discharges. LCIF was used in [19] to measure the electron density near the extraction aperture of a helium RF plasma cathode. Measurements with an intensified camera allowed generation of two-dimensional spatial maps of the electron density and the effective electron temperature that indicated the formation of a double layer sheath.

Computations of the electron density are also not straightforward, despite the availability of sophisticated numerical approaches and high-performance computational

resources. Especially at low pressures, when electron dynamics acquires a non-local character, kinetic simulations, like the Particle-in-Cell / Monte Carlo Collisions (PIC/MCC) are indispensable. For example, considering capacitively-coupled helium plasmas, PIC/MCC was used in [20] to study the structure of the discharge. The electron-energy distribution functions were found to be non-Maxwellian, and in the absence of secondary electron emission, electron heating in the sheath regions was enhanced at higher voltages compared to ohmic heating in the plasma bulk. In [21], it was shown that n_e scales approximately as the square of the frequency of the applied voltage and that by manipulating both frequency and voltage it is possible to control the ion current and energy independently. Heating mechanisms in collisionless sheaths were studied in [22], where it was found that energy loss from electrons escaping to the electrode can exceed the energy gain from sheath expansion heating if the ratio of the maximum sheath expansion velocity to the electron thermal velocity is too small, and that the electron inertia is an important factor in electron loss. In [23], a ring-shaped structured electrode was shown to increase n_e through the hollow cathode effect while maintaining high radial uniformity. Even though such PIC/MCC simulations can fully capture kinetic effects, they are susceptible to numerical heating effects [24, 25]. One of the quantities that these numerical effects influence most severely, especially in gases in which the elastic electron-impact cross section exhibits a Ramsauer-Townsend minimum, is indeed the electron density.

Besides these problems of simulations mentioned above, for accurate numerical results, the calculations need to consider the effects of atoms in the excited levels, too. Recently, a number of works have investigated the importance of such excited levels on argon discharges. In [26–28], e.g., a significant influence of the presence of these excited states on the plasma density was reported as well as an emerging dominance of the stepwise and pooling ionization processes when the pressure approaches the ≈ 750 mTorr (100 Pa) range. Beside collisional mechanisms, optical transitions between certain levels influence the populations of the excited levels, as well. Models that include both these effects are called collisional-radiative models (CRM) [29–33]. They are used primarily for diagnostic purposes by relating the experimental spectra to the plasma parameters such as the electron density and temperature.

In this work, we report comparisons of LCIF measurements and numerical modeling calculations of n_e and (effective) T_e in low-pressure capacitively-coupled radio-frequency discharges in helium gas. LCIF measurements up to 1000 mTorr are made using analytic functions fit to data generated by a CRM. Numerical modeling calculations are made using an extended PIC/MCC code and a diffusion-reaction-radiation model. A good agreement is found between the experimental and simulation results for n_e and a reasonable agreement is found for T_e . The simulations provide additional insights into the operation of the discharge at 100 mTorr and 1000 mTorr, including the density distributions of He^+ and excited He atoms, the rates of stepwise excitation and de-excitation processes and of stepwise ionization from He metastable levels, and the major populating and de-populating channels of He^+ and various He excited levels.

The paper is structured as follows: Section 2 describes the experimental methods. Section 3 describes the computational framework that consists of an extended PIC/MCC code (subsection 3.1) and a diffusion-reaction-radiation model (subsection 3.2). The experimental and modeling results are presented and compared in Section 4, while a summary is given in Section 5.

2. Experimental method

The experimental plasma source is a symmetric Capacitively-Coupled Plasma (CCP) cell, with a pair of stainless-steel electrodes of 14.2 cm diameter, placed at a distance of $L = 2$ cm or 4 cm from each other. The gas pressure is between $p = 50$ mTorr and 1000 mTorr and RF peak-to-peak voltages between $V_{pp} = 150$ V and 350 V are used at a frequency of $f = 13.56$ MHz. One of the electrodes is driven by a RF voltage

$$\phi(t) = 0.5 V_{pp} \cos(2\pi ft), \quad (1)$$

while the other electrode is grounded. Similar to previous work [34,35], care is taken to ensure a symmetric discharge suitable for comparison with 1d3v PIC/MCC simulation results, requiring equal powered and grounded surface areas around the plasma. The electrodes are placed at the center of a cylindrical borosilicate glass vacuum chamber (height 18 cm, outer diameter 16 cm, inner diameter 14.6 cm). The borosilicate glass is brazed to eight-inch conflat flanges on the top and bottom. The electrodes are held in place by stainless steel rods mounted through adjustable vacuum feedthroughs (Ultra-Torr to CF Flange Adapters) located on each flange. One of the flanges is driven by the RF voltage and the other is grounded, creating a symmetric CCP reactor. In asymmetric reactors, a DC self-bias voltage builds up due to differences in the grounded and powered surface areas and capacitive coupling with external grounded surfaces. In our reactor, the DC self-bias was measured to be less than 1% of V_{pp} , confirming the reactor is geometrically symmetric.

The chamber is evacuated to a base pressure of 7.5×10^{-8} Torr using a turbomolecular pump (Pfeiffer, HiPace 300) backed by a dry scroll pump (Edwards, nXDS6i). The operating pressure is set by limiting the pumping cross section with a gate valve and using a mass flow controller (MKS, 1179A00151CR18V), a capacitance manometer (MKS, Batartron), and a programmable interface controller (MKS, 946 Vacuum System Controller) to maintain the desired pressure through feedback control of the flow rate of high-purity helium gas (99.999% pure, 7-10 SCCM). The driving voltage is supplied by a linear power amplifier (Ophir, 5087RE) and waveform generator (Agilent, 33250A) via an impedance matching network (MFJ, MFJ-993B). The V_{pp} is measured by a high voltage probe (Teledyne Lecroy, PPE6kV-A), tuned to operate at 13.56 MHz, and a 1 GHz oscilloscope (Teledyne Lecroy, HDO6104). Visual observation confirmed that no plasma is created outside the region of the electrode gap. This stable mode of operation is ensured by having only narrow gaps between the electrode edges and the glass walls of the vacuum chamber.

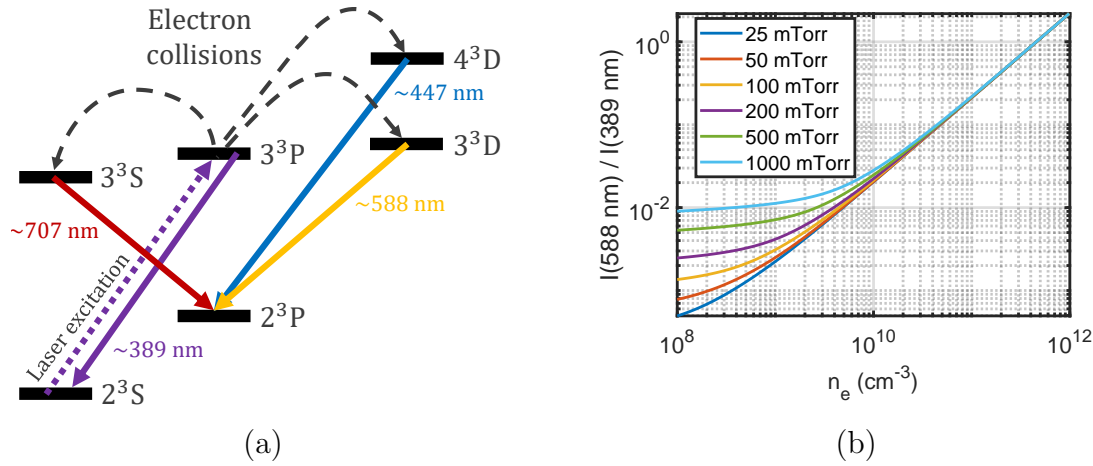


Figure 1. Helium LCIF. (a) A laser tuned near 389 nm excites electrons from the metastable 2^3S state to the 3^3P state. Spontaneous emissions at 588 nm and 447 nm then contain information about n_e and T_e . (b) Calibrations derived using the CRM [36] that are used to determine n_e from the measurement data.

The LCIF method is an extension of the Laser Induced Fluorescence (LIF) technique. Considering figure 1(a), both LIF and LCIF employ a laser to excite atoms in the plasma from a lower-lying level (2^3S) to a higher-lying level (3^3P). In LIF, the radiation emitted from the atoms as these decay spontaneously from the higher-lying level (3^3P) to a lower-lying level (2^3S) can be measured to determine the relative density of the atoms in the lower-lying level. In the case of LCIF, in addition to monitoring the LIF signal from 3^3P , the emission is also monitored from additional levels, which are close to 3^3P (3^3D and 4^3D) but have somewhat higher energy. These excited levels are populated primarily via collisions between the laser excited species (3^3P) and free electrons. Knowledge of these interactions are used in a CRM [36] to determine information about n_e and T_e .

To excite LIF and LCIF, pulsed laser light is supplied by a tunable laser source (EKSPLA, NT230) consisting of a Nd:YAG laser, optical parametric amplifier, and a sum-frequency generator. The laser wavelength is tuned near 389 nm, providing up to 1.7 mJ of energy per pulse at a repetition rate of 50 Hz and a pulse width of 3 ns. The laser beam is expanded to 5 cm diameter and then focused into a light sheet with a width of approximately $125 \mu\text{m}$ at the center of the CCP cell using a cylindrical lens. An intensified camera (Andor, iStar DH334T), oriented perpendicular to the laser light sheet, is used to image the LIF and LCIF emission through a telecentric lens (Edmund Optics, 62-922, working distance 18.2 cm) and bandpass filters (10 nm bandwidths) centered at appropriate wavelengths (387 nm, 589 nm, and 445 nm; Edmund Optics, 84-110, 65-223, and 34-501, respectively). A fiber-coupled spectrometer (StellarNet, BlueWave) is used to measure the optical emission spectra of the discharge and confirm that the bandpass filters allow discrimination of the respective line emissions. The telecentric lens is positioned at its working distance from the center of the discharge.

The bandpass filters are placed between the telecentric lens and the intensified camera, ensuring normal incidence of the chief light rays and minimal distortion of the bandpass filter transmission curves. The intensified camera, telecentric lens, and bandpass filter are mounted on an optical breadboard that is adjusted using a linear translation stage for each filtered wavelength to correct for minor changes in the working distance due to chromatic aberration. The relatively large depth of field and uniform magnification of the telecentric lens nearly eliminates effects of chromatic aberration and reflections of LIF and LCIF emission from the electrode surfaces. This configuration of the laser light sheet, intensified camera, telecentric lens, and bandpass filters allows imaging of LIF and LCIF across the entire discharge gap at the center of the discharge. For safety, an enclosure box is built around the CCP with walls located at least 10 cm away from the vacuum chamber. Black cardboard (Thorlabs, TB5) is mounted on the inner walls of this safety enclosure to prevent measurements of reflected light. The vacuum chamber, safety enclosure box, and the intensified camera are mounted together on a motorized linear translation stage to enable precise alignment with the pulsed laser light sheet.

Acquisition time varies for the three filtered wavelengths, 389 nm (4-40 seconds), 588 nm (30-400 seconds), and 447 nm (175-1500 seconds), with longer acquisition times required for smaller n_e at lower pressures and lower V_{pp} . The relatively long acquisition time at 447 nm is due to a lower electron impact excitation rate ($\approx 10^{-5} \text{ cm}^3\text{s}^{-1}$ for 3^3P to 3^3D and $\approx 3 \times 10^{-7} \text{ cm}^3\text{s}^{-1}$ for 3^3P to 4^3D [36]). The waveform generator in the RF power source is synchronized to a delay generator (Stanford Research Systems, DG645) that then triggers the laser source and the intensified camera at 50 Hz, allowing measurements of LCIF at various phases of the RF cycle. In this work, all measurements are time-averaged over the entire RF cycle. The camera gate width is fixed at 50 ns with a delay of 50 ns with respect to the laser pulse. The camera gain is fixed at 2500 (4095 max), which is found to give the best quality images. The number of accumulations is calculated by multiplying the acquisition times by 50 Hz: 389 nm (200-2000), 588 nm (1500-20000), and 447 nm (8750-75000).

Measurements are made at 389 nm (3^3P to 2^3S), 588 nm (3^3D to 2^3P), and 447 nm (4^3D to 2^3P) with the intensified camera equipped with one of the three bandpass filters. At each wavelength, the different transmissions and detection efficiencies of the glass chamber, telecentric lens, bandpass filters, and intensified camera are measured using a broadband light source and monochromator and are corrected for in post-processing. The different acquisition times at each wavelength are also corrected for in post-processing. For each bandpass filter, three images are acquired by the intensified camera. The first image corresponds to background signal of the plasma light emission without the laser probe. The second image corresponds to background signal without plasma light emission but with the laser probe. These first two images are subtracted from the third image acquired with plasma light emission and the laser probe to provide the pure LIF and LCIF signals. The CRM developed by Barnat and Frederickson [36] is used to determine n_e and T_e from the measurements. The CRM considers 14 states in the helium triplet manifold and the ground state, leading to 15 coupled differential

equations that are solved using a stiff low-order ODE solver in MATLAB. The CRM assumes a Maxwellian energy distribution for the electrons. Interactions that can cause electron state transfers between the singlet and triplet states are ignored. For atom to atom collisions, only interactions between the various excited states and the helium ground state are considered. The time dependence of the pulsed laser excitation is incorporated as an effective Einstein coefficient accounting for effects of light absorption and stimulated emission. For a given n_e , T_e , and helium gas pressure, the equilibrium distribution of excited states is determined and then perturbed by a 3 ns wide laser pulse that excites the 2^3S to 3^3P transition. The time-integrated light emission that is detected by the intensified camera at 389 nm, 588 nm, and 447 nm is then calculated. For each image pixel, n_e is calculated from the $I(588 \text{ nm})/I(389 \text{ nm})$ ratio and T_e is calculated from both the $I(588 \text{ nm})/I(389 \text{ nm})$ and $I(447 \text{ nm})/I(588 \text{ nm})$ ratios. More information about the CRM can be found in [36].

The uncertainty in n_e can be approximated using a three-level LCIF model [16], where n_e can be written as [19]

$$n_e = \frac{F_j A_1 \epsilon_1 \lambda_j}{A_j \epsilon_j \tau_j \lambda_1 K_j} - \frac{R_{j,at}}{K_j}, \quad (2)$$

where subscript 1 denotes the LIF transition from 3^3P to 2^3S , subscript j denotes the LCIF transition from 3^3D to 2^3P , F_j is the $I(588 \text{ nm})/I(389 \text{ nm})$ ratio, A is the spontaneous emission rate, ϵ is the detection efficiency, λ is the wavelength of the transition, K_j is the rate constant for electron impact excitation from state 1 to state j , τ_j is the total depopulation rate of state j due to spontaneous, electronic, and atomic processes, and $R_{j,at}$ is the population rate of state j due to atom-atom collisions. Systematic bias in the absolute value of n_e is dominated by the uncertainty in the quantities K_j , τ_j , and $R_{j,at}$, estimated as 50% [19].

Figure 1(b) presents the calibrations derived using the CRM that are used to determine n_e from the measurement data. At pressures below 200 mTorr and for n_e above 10^9 cm^{-3} , the effect of the $R_{j,at}$ term in eq. 2 is small and n_e increases at a nearly linear rate with F_j , a key feature of the LCIF diagnostic. In this work, LCIF measurements are made at pressures where atom-atom collisions cause a deviation from this ideal linear behavior. For this reason, as presented in Appendix A and figure 1(b), CRM predictions are fit to analytic functions that are used to convert the $I(588 \text{ nm})/I(389 \text{ nm})$ and $I(447 \text{ nm})/I(588 \text{ nm})$ ratios to n_e and T_e . It is important to note that estimates of T_e using the CRM rely on the assumption of a Maxwellian energy distribution for the electrons. Deviations from this assumption complicate the quantitative determination of T_e from the LCIF data. Results should therefore be considered as effective temperatures that correspond to the observed LCIF for the idealized Maxwellian plasma. A non-Maxwellian distribution is expected to have little to no effect on the calculation of n_e because the small energy spacing between the 3^3P and 3^3D states causes the 3^3P to 3^3D transition to be insensitive to T_e and the electron energy [36].

3. Computational method

The numerical studies are based on a hybrid computational framework (see figure 2), which consists of (i) a Particle-in-Cell / Monte Carlo Collisions (PIC/MCC) code and (ii) a Diffusion-Reaction-Radiation (DRR) code. In the PIC/MCC module, electrons can collide not only with ground state He atoms (as in conventional PIC/MCC simulations), but also with He atoms in several excited levels with spatial density distributions specific for each of the levels. This way, the rates of all direct and stepwise, as well as de-excitation electron-impact collisions are derived. These rates are coupled from the PIC/MCC module to the DRR module that solves the diffusion equations of the He atoms in the excited levels, considering their sources and losses, which includes the rates of the electron-impact processes (derived by the PIC/MCC code) as well as the rates of the radiative transitions between the various levels and pooling ionization. The computed (spatially dependent) densities of the He atoms in the excited levels are fed back to the PIC/MCC module and the two modules, which will be described below to some detail, are executed iteratively, as shown in figure 2, until the converged solution is obtained. The elementary processes taking place in the gas volume and at the electrode surfaces are listed in table 1.

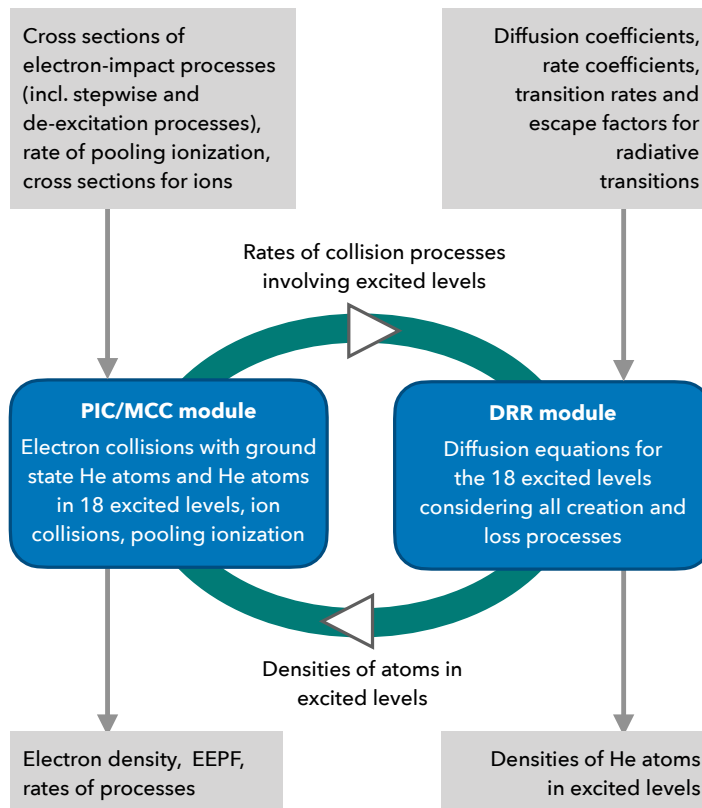


Figure 2. Scheme of the computational framework, showing the two modules and their input / output data.

Table 1. Gas-phase elementary processes considered in the model. Here, He^* and He^{**} denote excited levels, with $\varepsilon(\text{He}^*) < \varepsilon(\text{He}^{**})$. He^r and He^m represent the lowest resonant (2^1P) and the metastable (2^1S and 2^3S) levels, respectively. GS stands for the ground state. For the processes involving radiation, '×2' indicates that both spontaneous emission and re-absorption processes are considered.

reaction	name	# of processes	Ref.
$e^- + \text{He} \rightarrow e^- + \text{He}$	elastic scattering	1	[37]
$e^- + \text{He} \rightarrow e^- + \text{He}^*$	direct excitation	18	[38]
$e^- + \text{He} \rightarrow 2e^- + \text{He}^+$	direct ionization	1	[38]
$e^- + \text{He}^* \rightarrow e^- + \text{He}$	de-excitation to GS	18	see text
$e^- + \text{He}^* \rightarrow e^- + \text{He}^{**}$	stepwise excitation	153	[38]
$e^- + \text{He}^{**} \rightarrow e^- + \text{He}^*$	de-excitation to excited levels	153	see text
$e^- + \text{He}^* \rightarrow 2e^- + \text{He}^+$	stepwise ionization	18	[38]
$\text{He}^m + \text{He}^m \rightarrow e^- + \text{He}^+ + \text{He}$	pooling ionization	3	[39]
$\text{He}^+ + \text{He} \rightarrow \text{He}^+ + \text{He}$	elastic scattering (isotropic + backward)	2	[40]
$\text{He}^* \leftrightarrow \text{He} + \text{photon}$	spont. em. & re-abs. to/from GS	3 (×2)	[41]
$\text{He}^{**} \leftrightarrow \text{He}^* + \text{photon}$	spont. em. & re-abs. between exc. levels	34 (×2)	[41]
$\text{He}^* + \text{wall} \rightarrow \text{He} + \text{wall}$	diffusion to boundaries	18	[33, 39]

3.1. The PIC/MCC module

The PIC/MCC module implements a 'classical' 1d3v (one-dimensional in real space and three-dimensional in velocity space) electrostatic simulation of the kinetics of electrons and He^+ ions in a discharge chamber equipped with two plane-parallel electrodes. The code includes, however, an important extension to conventional PIC/MCC simulations: besides ground state (GS) He atoms, He atoms in 18 excited levels are also considered as targets in electron-neutral collisions.

The elastic (momentum transfer) cross section for e-He collisions is taken from LxCat [42] (Biagi Magboltz, version 8.97) [37], while the inelastic 'level-to-level' e-He cross sections are adopted from [38]. We consider excited levels included in tables 1-3 of [38] (i.e., those with principal quantum numbers not exceeding 4) for the direct (i.e., from GS) excitation and stepwise excitation processes. The cross sections of the reverse reactions of the excitation processes are computed based on the principle of detailed balance (see, e.g., [43]). Direct, as well as stepwise ionization reactions listed in table 4 of Ref. [38] (except double ionization) are taken into account in the model. Besides these ionization channels, pooling ionization becomes important as well at enhanced densities of the metastable levels. The rate coefficient of this reaction is adopted from [39]. For the He^+ ions we consider elastic (isotropic and backward) scattering based on the data of Phelps [40].

The spatial distributions of the densities of the He atoms in the various excited levels are provided by the calculations in the DRR module, while the GS He atoms are uniformly distributed within the electrode gap, with a density n_{gas} corresponding to the prescribed gas pressure, p , and temperature, T_g (taken to be 300 K). This assumption

of a homogeneous gas density distribution is justified by the moderate increase of gas temperature observed under similar conditions in an argon CCP [35] and by the fact that helium is a much better thermal conductor as compared to argon. The depletion of the GS atom density by the presence of the excited He atoms is negligible and is, thus, disregarded.

In the PIC/MCC simulation, an equidistant spatial grid with $N_g = 500$ points is used for the calculation of the charged particle densities and the electric potential. The RF cycle is divided into N_t time steps for the integration of the equations of motion of the electrons (via the leapfrog scheme) with a time step of $\Delta t_e = T_{\text{RF}}/N_t$. N_t ranges between 2000 and 4000 depending on the gas pressure. For the ions, subcycling is used with a time step of $\Delta t_i = 20\Delta t_e$. These settings respect the stability and accuracy criteria of the PIC/MCC scheme [44–46].

The surface model in the PIC/MCC code includes electron emission induced by He^+ ions and He^m metastable atoms. For the ions, a secondary electron yield of $\gamma_i = 0.3$ is adopted based on [47]. For the metastables atoms, we take $\gamma_m = \gamma_i$ based on the findings of [48] where similar yields for these species were found. For the VUV photons reaching the electrodes, an electron yield of $\gamma_p = 0.1$ is assumed. The electrons reaching the electrode surfaces are assumed to be elastically reflected with a probability of $r = 0.7$ [5, 35].

During the execution of a given number of RF cycles in the PIC/MCC simulation, spatially resolved data for the rates of the electron-impact processes (including direct and stepwise excitation and ionization, as well as de-excitation) are calculated by computing the collision frequencies of the respective processes along the trajectories of individual electrons traced in the simulation. The data are interpolated to a grid consisting of $N_f = 60$ points, which provides high enough spatial resolution. These time-averaged rates, which are the primary output of the PIC/MCC simulation (see figure 2), are written to a data file, which is subsequently read by the DRR module.

3.2. The DRR module

The core of the DRR module is a set of spatially one-dimensional time-dependent differential equations for the diffusion of the He atoms in the 18 excited levels considered:

$$\frac{\partial n_k}{\partial t} = D_k \frac{\partial^2 n_k}{\partial x^2} + S_k(x), \quad (3)$$

where n_k is the density and D_k the diffusion coefficient of species $k = 1 \dots 18$, and $S_k(x)$ is the net source function that includes the rates of all creation and loss channels for the given species (see, e.g., [27]). It is noted that diffusion is appreciable only for the long-lifetime (i.e., metastable) species, for these, $D = 8.992 \times 10^{-6} T_g^{1.5}/(p/133.3)$ (with T_g in units of K and p in units of Pa) is taken from [39].

The set of the above equations is solved with an explicit, finite difference forward-time-centered-space (FTCS) method [49], for the stationary state as in [27], with a

boundary condition

$$-D_k \frac{\partial n_k}{\partial x} = \frac{\gamma_k}{2(2 - \gamma_k)} n_k \bar{v}_k, \quad (4)$$

where γ_k is the recombination coefficient and \bar{v}_k is the mean velocity of species k at the surface. For γ_k a value of 0.5 is adopted [27]. The diffusion equations are solved for the steady state.

The contributions of the electron-impact processes to the temporally averaged (over several RF periods) source functions appearing in eq. (3) are obtained in the PIC/MCC module. In addition to these, the rates of radiative transitions and the rate of the pooling ionization process are also included in the net source terms. Although the discharge model is one-dimensional, in order to approximate better the cylindrically symmetric geometry of the experimental system, the radial diffusion losses of the species are also taken into account via a loss frequency defined by their diffusion coefficients and the chamber radius.

The set of radiative transitions is adopted from the work of Drake and Morton [41] along with the corresponding oscillator strength values. To account for the partial trapping of the spectral lines, we adopt the use of an escape factor, which allows a simplified treatment of the radiation trapping. Based on the geometry of the plane-parallel electrode arrangement, we use an escape factor appropriate for a slab geometry [50,51]. (More precisely, we use eqs. (6a) and (6b) of [51], which originate from [50], but in [51] typographical errors of the corresponding equations of [50] have been corrected.) We note that the escape factor used here was derived for Doppler broadening of the spectral lines [51], for the low-pressure conditions studied here this line broadening mechanism is dominant. For the conditions of this study, we find escape factor values in the range of $10^{-3} - 10^{-4}$ for the first resonant line and values in the range of $0.2 - 1.0$ for the other transitions.

In addition to the calculation of the populations of the He atoms in the excited levels, the intensity of the radiation can also be derived in the DRR module. As the light from the plasma is detected perpendicularly to the discharge axis, another escape factor (η^*), appropriate for a cylindrical geometry [52], is used for the computation of the spectral line intensities:

$$I_{j \rightarrow i} = n_j A_{j \rightarrow i} \eta_{j \rightarrow i}^*, \quad (5)$$

where $A_{j \rightarrow i}$ represents the Einstein coefficient of the $j \rightarrow i$ transition.

3.3. Coupling of the codes

As already mentioned in section 3, the PIC/MCC and the DRR codes are executed iteratively to obtain a converged solution for a given set of discharge conditions. This convergence is usually achieved after a few thousands RF cycles, similarly to 'standard' PIC/MCC simulations.

The main results of the simulations (points of comparison with the experiments) are the electron density distribution, $n_e(x)$, the spatially resolved electron temperature,

$T_e(x)$, which is obtained from the simulation as an effective value derived from the mean electron energy ($T_e(x) = 2\langle\varepsilon_e(x)\rangle/(3k_B)$), as well as the spatial distribution of the plasma radiation on selected He atomic lines.

4. Results

The results of the measurements and the calculations for the spatial distribution of the electron density are compared in figure 3. Panels (a), (b), and (c), present, respectively $n_e(x)$ for peak-to-peak voltages of $V_{pp} = 350$ V, 250 V, and 150 V, for $L = 4$ cm electrode gap and pressures between $p = 50$ mTorr and 1000 mTorr. Data for $L = 2$ cm electrode gap are displayed in panel (d) for $V_{pp} = 350$ V and for pressures between $p = 250$ mTorr and 1000 mTorr.

We find a fairly good agreement between the experimental and computational results for the electron density. In the inner, bulk part of the plasma, the error in n_e measured by LCIF is dominated by uncertainty in K_j , τ_j , and $R_{j,at}$, and is estimated as 50%. This uncertainty is consistent with previous comparisons of LCIF to double probe measurements [36]. Similarly, the error in n_e computed by PIC/MCC is dominated by uncertainty in the rates of the elementary processes listed in table 1 (originating from uncertainties of cross sections and rate coefficients) and is estimated to be up to 50%. Considering figure 3, in the bulk plasma near the middle of the discharge gap, the experimental and computed n_e agree within the expected errors, except at the lowest pressures (50 mTorr at $L = 4$ cm or 250 mTorr at $L = 2$ cm). At 4 cm electrode gap the experiment tends to result in somewhat higher electron density in the bulk as compared to the numerical prediction. At 2 cm gap, this is only true at the highest pressure of 1000 mTorr, at lower pressures the simulations yield higher densities than the experiments. The cause of the disagreements at the lower pressures is not clear. However, these conditions are near the minimum maintaining pressure/voltage of the discharge, where we may expect uncertainties in the calculated rates of the elementary processes to amplify, increasing the computational errors. Likewise, due to the lower electron density at these conditions, the measurements are also expected to have a larger uncertainty due to a lower signal to noise ratio.

Considering the sheath regions in figure 3, the experimental n_e values are consistently lower compared to the computed ones, except at the two highest pressures (500 mTorr and 1000 mTorr) in the 4 cm electrode gap, where this behavior reverses. There are two additional sources of error in the LCIF diagnostic in the sheath regions. First, when T_e is around 20 eV, as occurs in the sheath regions (discussed below), using the CRM, we find that the calibration in figure 1(b) under-predicts n_e by 75%, explaining why the experimental n_e values are consistently lower compared to the computed ones at lower pressures. A second error is introduced at the two highest pressures (500 mTorr and 1000 mTorr). The measured intensity ratio, $I(588 \text{ nm})/I(389 \text{ nm})$, was found to fluctuate by up to 10% in the sheath regions over repeated measurements, which creates 50% uncertainty in n_e due to the shape of the calibration curve in figure 1(b) in the region

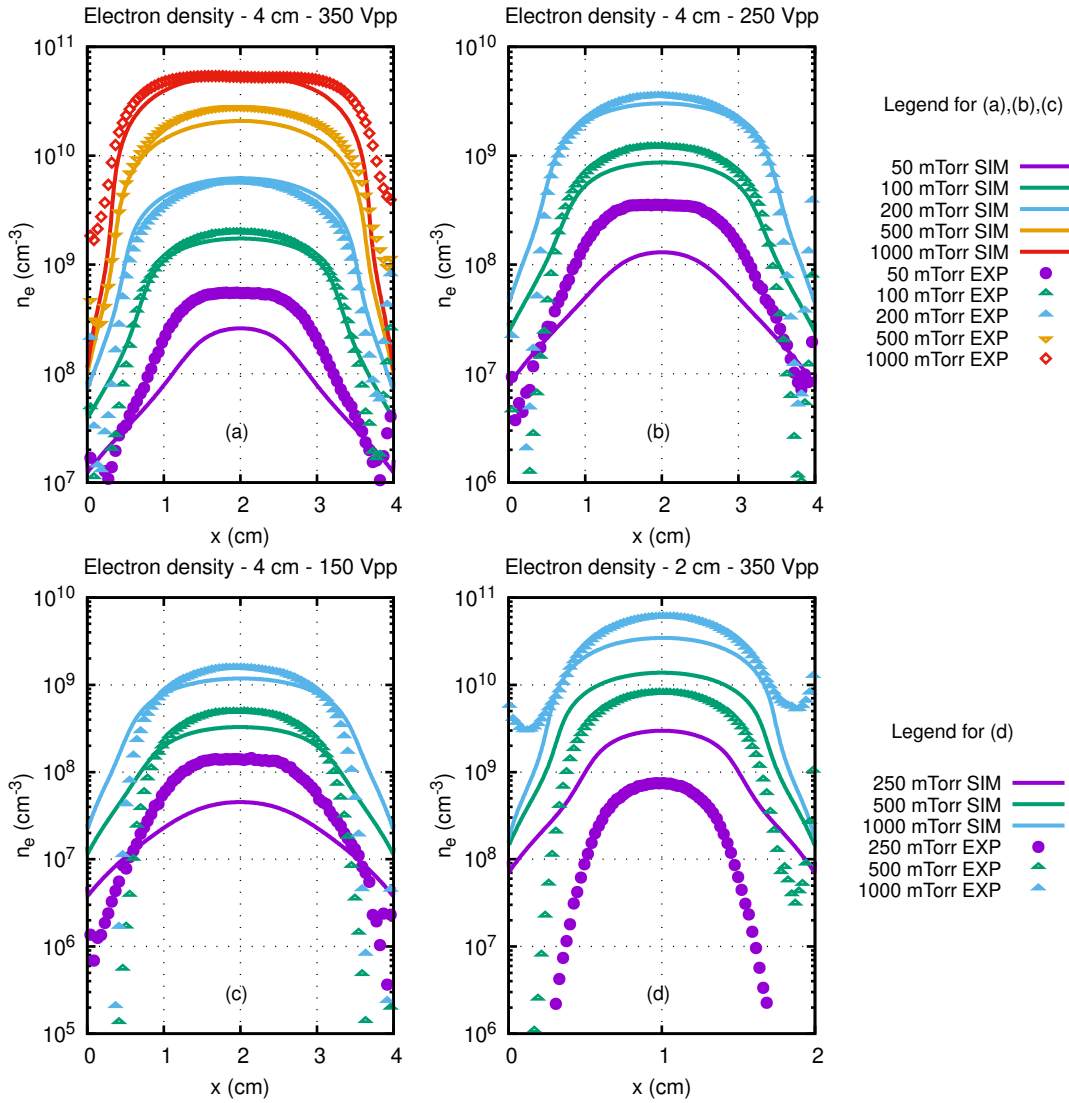


Figure 3. Comparison of the electron density data obtained from the experiments ("EXP") and the simulations ("SIM") for different pressures, for $L = 4$ cm at different V_{pp} ((a)-(c)) and for $L = 2$ cm and $V_{pp} = 350$ V (d)

of n_e less than 10^{10} cm^{-3} , giving a total experimental error of up to 175% in the sheath regions in the worst case. Differences between the experimental and computational results increase with decreasing pressure and V_{pp} , and are greater than 175% near the minimum maintaining pressure/voltage of the discharge, as already discussed. We find that, at 100 mTorr, the sheath lengths range between approximately 1.5 cm and 0.8 cm (in the order of increasing driving voltage). The sheath length decreases with further increasing pressure to reach about 0.3 cm at 1000 mTorr pressure and 350 V_{pp} .

The comparison of the spatial distributions of the electron temperature, $T_e(x)$, obtained from the measurements and the computations is shown in figure 4. For the 4 cm electrode gap we find the best agreement at the lowest pressure of 50 mTorr, with

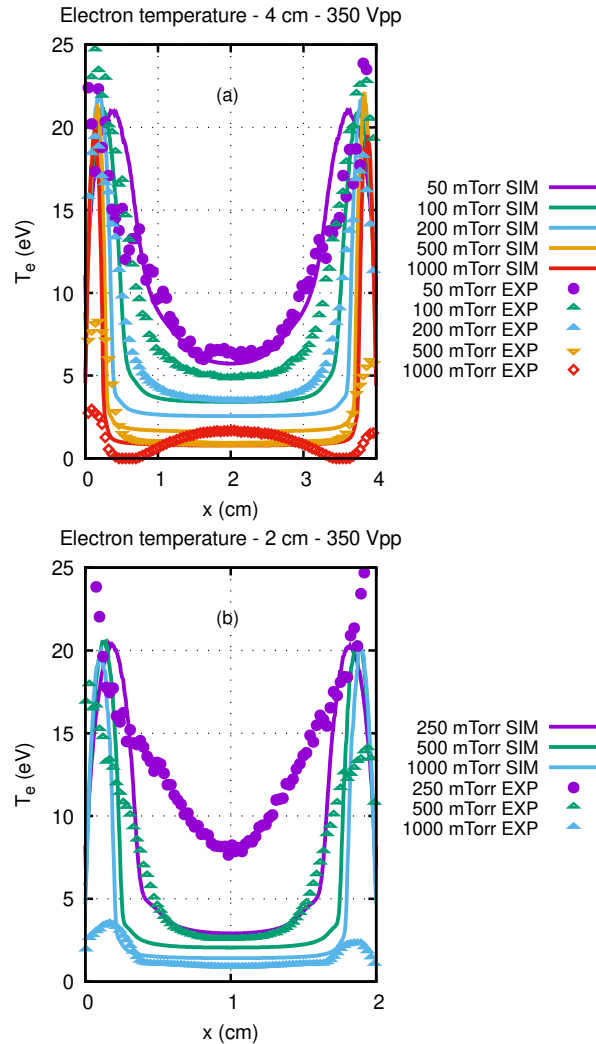


Figure 4. Comparison of the electron temperature data obtained from the experiments ("EXP") and the simulations ("SIM") for $L = 4$ cm (a) and for $L = 2$ cm at $V_{pp} = 350$ V (b).

very nearly matching bulk electron temperature values around 6 eV, and values reaching $\approx 20 - 25$ eV in the sheath domains. With increasing pressure the differences increase both in the bulk and in the sheaths. For the 2 cm gap, the simulation yields significantly lower values as compared to the measured ones, amounting about a factor of two at the lowest pressure. The agreement between the T_e values in the bulk improves at higher pressures, but in the sheath regions the computed values become significantly higher than the experimental results at 1000 mTorr, similarly to the case of the 4 cm gap. These differences are caused by a number of factors. The energy distributions of the electrons deviate from the Maxwellian energy distributions assumed in the CRM that was used to determine $T_e(x)$ from the experimental data. Compared to n_e in eq. (2), the uncertainty in T_e is approximated using a four-level system and is more sensitive to errors in populating and depopulating rates. Finally, as discussed above, differences

in the sheath regions at 500 mTorr and 1000 mTorr are caused by small errors in both n_e and $I(447 \text{ nm})/I(588 \text{ nm})$ having relatively large influences on the interpolated value of T_e (see figure A1). We estimate the error in electron temperature (electron mean energy) measured by LCIF as 100% in the plasma bulk, 100% in the sheath regions at pressures less than 200 mTorr, and 500% in the sheath regions at pressures above 200 mTorr.

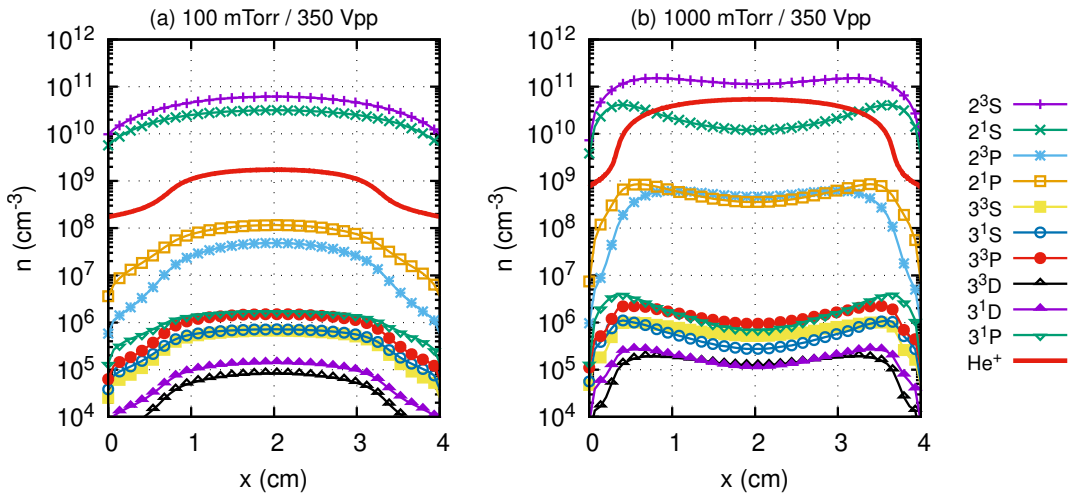


Figure 5. Computed density distributions of the He atoms in excited levels with $n \leq 3$ and the He^+ ion density distribution for 100 mTorr (a) and 1000 mTorr (b), at $V_{pp} = 350 \text{ V}$, and $L = 4 \text{ cm}$ discharge conditions.

The simulations provide further insights into the operation of the discharge and in the following, some of the plasma characteristics (most of which are not accessible experimentally) will be illustrated for 100 mTorr and 1000 mTorr pressures, $V_{pp} = 350 \text{ V}$, and $L = 4 \text{ cm}$, based on the next figures. Figure 5 depicts the densities of the He atoms in various excited levels with a principal quantum number $n \leq 3$ and the He^+ ion density. Figure 6 shows the direct electron-impact creation rates of the He atoms in all the excited levels considered in the model and the ionization rate. Finally, figure 7 presents the rates of the more important stepwise excitation and de-excitation processes and the electron-impact stepwise ionization rates from the metastable levels.

In figure 5, we find that at $p = 100 \text{ mTorr}$ the 2^3S and 2^1S metastable atoms have a peak density that is about an order of magnitude higher as compared to the He^+ ion density (being $\approx 10^9 \text{ cm}^{-3}$) in the plasma bulk. The levels with the next highest populations are 2^1P and 2^3P , with densities an order of magnitude below the ion density. The levels with $n > 2$ exhibit densities below $\approx 10^6 \text{ cm}^{-3}$. At $p = 1000 \text{ mTorr}$, the ion density increases significantly, to the proximity of 10^{11} cm^{-3} . The density of the He 2^3S metastable atoms is still about a factor of two higher than the ion density in the center of the discharge. The density of the singlet 2^1S metastables, however, departs remarkably from that of the triplet 2^3S metastables. This depletion is mainly due to two effects: (i) the decreasing rate of production of 2^1S as compared to 2^3S at the

higher pressure (see figure 6), and (ii) the onset of the stepwise electron impact $2^1S \rightarrow 2^3P$ excitation process that depopulates the singlet metastable level (see figure 7). At these conditions, the densities of the 2^1P and 2^3P atoms approach 10^9 cm^{-3} , while the densities of atoms with $n > 2$ are still in the range of $10^5 - 10^6 \text{ cm}^{-3}$, not exceeding significantly the corresponding values found at 100 mTorr.

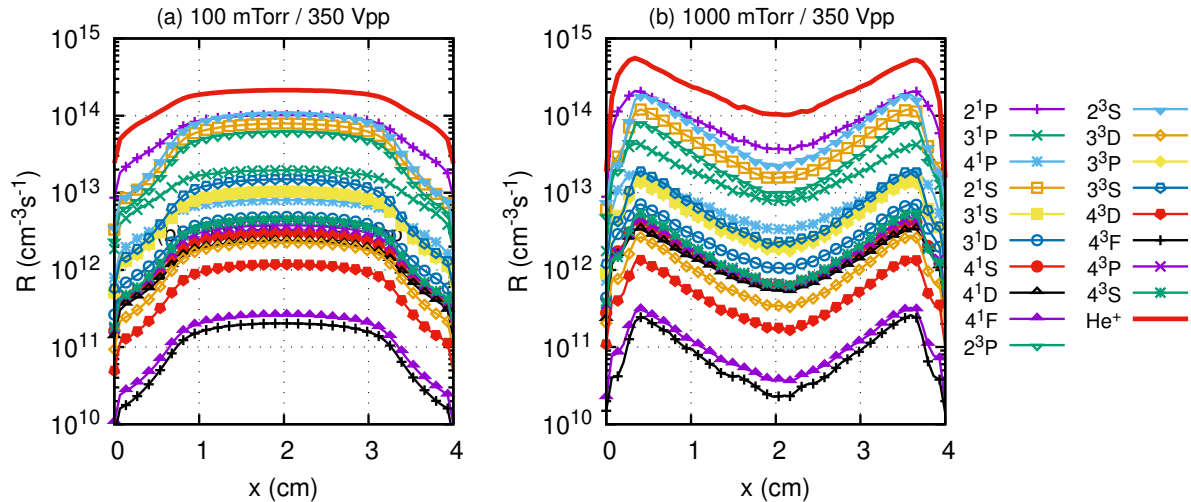


Figure 6. Computed direct electron-impact excitation rate of ground-state He atoms to excited levels with $n \leq 3$ and the direct ionization rate for 100 mTorr (a) and 1000 mTorr (b), at $V_{pp} = 350 \text{ V}$, and $L = 4 \text{ cm}$ discharge conditions.

At 100 mTorr, the electron-impact excitation rates and the ionization rate (R) exhibit a broad maximum within the plasma bulk, as revealed in figure 6(a). Among the excitation rates, the ones leading to He atoms in the $n = 2$ group are dominant, the additional levels are populated by at least an order of magnitude lower rates. At the higher pressure of 1000 mTorr, the $R(x)$ functions become convex in the center of the discharge due to the decreased width of the sheaths. It is worth noting that the 3^1P excitation rate is enhanced to a value characteristic of the $n = 2$ levels.

Regarding the stepwise excitation and ionization processes, some of which are shown in figure 7, only the $2^3S \rightarrow 2^3P$ and $2^1S \rightarrow 2^1P$ processes appear to have appreciable rates at 100 mTorr. At 1000 mTorr the situation changes considerably: besides the processes mentioned above, the $2^1S \leftrightarrow 2^3S$ metastable conversion processes and the $2^1S \rightarrow 2^3P$ as well as the $2^3S \rightarrow 2^1P$ singlet \leftrightarrow triplet processes acquire higher rates. Stepwise ionization from the metastable levels remains insignificant at both pressures considered here, due to their rates being about two orders of magnitude lower as compared to the direct electron-impact ionization of ground-state He atoms (cf. figure 6).

Figures 8 and 9 present temporally and spatially averaged rates of the most important elementary processes in the plasma. These data allow identification of the dominant electron impact (direct and stepwise) excitation processes and radiative decay processes, as well as quantification of the weights of the various ionization channels, i.e., the major pathways of the ‘global’ flow of energy in the system. Figure 8 presents data

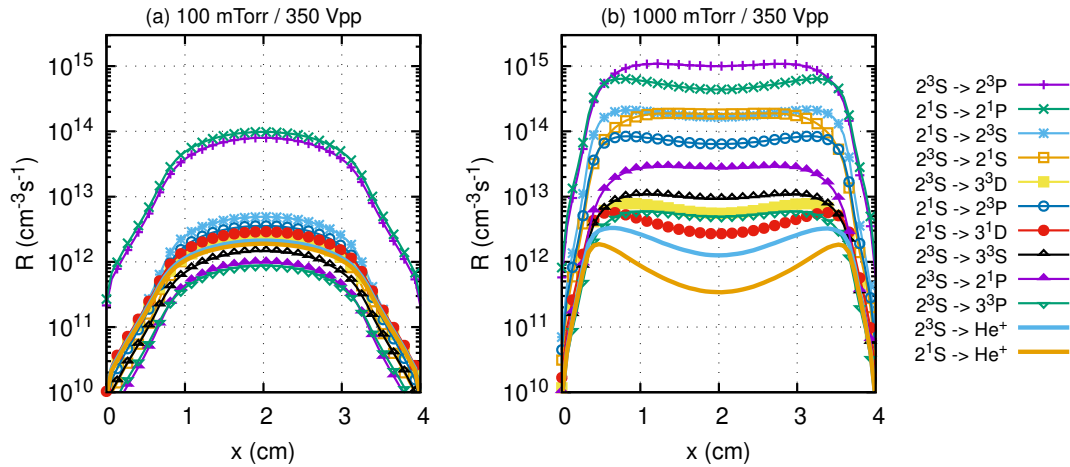


Figure 7. Rates of important stepwise excitation and de-excitation processes and of the stepwise ionization from the He metastable levels for 100 mTorr (a) and 1000 mTorr (b), at $V_{pp} = 350$ V, and $L = 4$ cm discharge conditions.

for $p = 100$ mTorr, $V_{pp} = 350$ V, while figure 9 displays the results for $p = 1000$ mTorr, $V_{pp} = 350$ V. Although the calculations cover all excited levels up to the principal quantum number of $n = 4$, here only levels with $n \leq 3$ are shown, with the exception of the 4^3D level, which is also relevant for the LCIF measurements. The $n = 4$ levels, in general, play a minor role in the flow of energy in the system. Figure 8 reveals that from the He ground state the 2^3S , 2^3P triplet and the 2^1S , 2^1P singlet levels are most heavily excited by electron impact. The coupling between the 2S and 2P levels appears to be dominant within both (i.e., singlet and triplet) systems: the 2P levels are strongly populated from the 2S levels by stepwise electron impact excitation, while strong radiative transitions represent the backward path. For the 2^1P level, the loss due to resonant radiation is significant, too. There is marginal electron-impact coupling between the singlet and triplet system of levels. Concerning ionization, the major source is direct electron impact, pooling processes cause about 1/6 part of ionization, while stepwise ionization is negligible (as already mentioned earlier). The transitions observed in the LCIF experiment are rather weak in the absence of laser excitation as compared to the strongest near-infrared $2P \rightarrow 2S$ transitions.

At higher pressure, the coupling of the excited levels becomes stronger as illustrated in figure 9 for the case of $p = 1000$ mTorr, $V_{pp} = 350$ V, $L = 4$ cm. Here, besides the 2S and 2P levels, the 3^1P level is also heavily populated by electron-impact excitation from the ground state. The most striking difference, however, is the appearance of strong stepwise excitation channels between the triplet/singlet 2S and 2P levels (i.e. $2^1S \rightarrow 2^3P$ and $2^3S \rightarrow 2^1P$). The importance of the pooling ionization increases as well at this high pressure, amounting about 1/3 of the total ionization at the conditions shown in figure 9.

The data obtained from the DRR model for the various electron-impact and radiative processes, some of which was already presented in figures 8 and 9 also allow

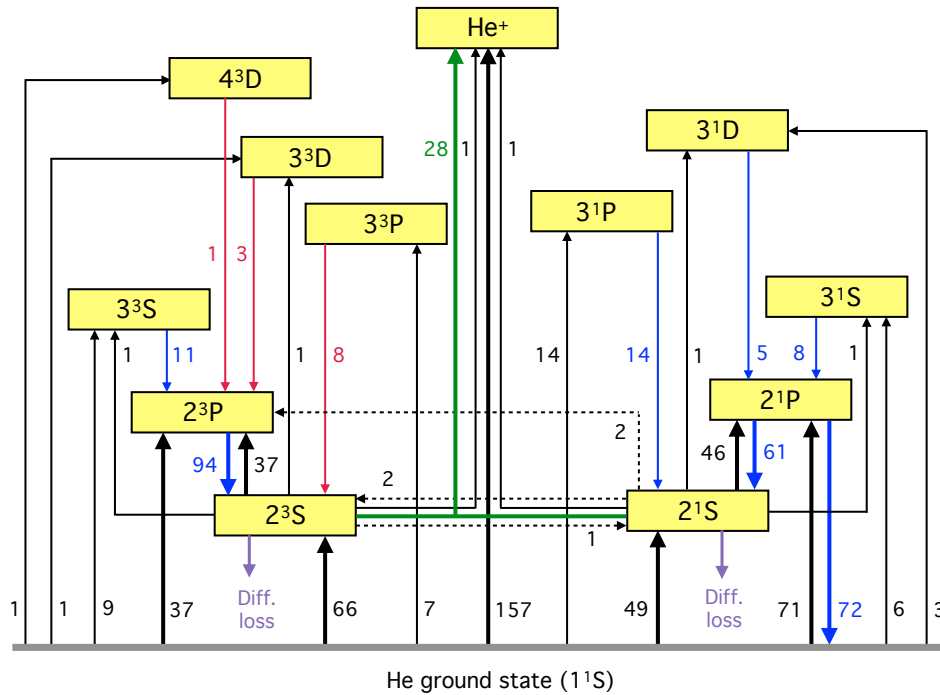


Figure 8. Major populating and de-populating channels of various He* (excited) levels and He⁺. The numbers indicate spatially averaged (and rounded to an integer number) rates in units of $10^{12} \text{ cm}^{-1} \text{ s}^{-1}$. Discharge conditions: $p = 100 \text{ mTorr}$, $V_{pp} = 350 \text{ V}$, $L = 4 \text{ cm}$. The black lines represent electron-impact collisions, among these the dotted lines indicate singlet \leftrightarrow triplet channels. Blue and red lines are radiative transitions, red color indicates the transitions involved in the LCIF emission measurements. Green lines correspond to pooling ionization. Thick lines mark the most significant mechanisms. The purple arrows denote diffusion of the metastable levels. Excited levels only up to principal quantum numbers of $n \leq 3$ are shown except the 4^3D level that is also relevant for the LCIF measurements. The slightly inaccurate balance of rates (small difference between the total ‘incoming’ rates and total ‘outgoing’ rates) for specific levels originates from rounding errors and the omission of excitation/de-excitation/radiative channels with low rates.

a comparison of the spectral line intensities with experimentally observed values. The line intensities are calculated – as explained in section 3.2 – using eq. (5), based on the population of the upper level, and the respective values of the Einstein coefficient of the given transition and the escape factor. The latter is found to be close to 1 for most of the transitions, i.e., self-absorption is negligible for most of the spectral lines even at the highest pressure of 1000 mTorr. Exceptions are the near-infrared $2^3\text{P} \rightarrow 2^3\text{S}$ and $2^1\text{P} \rightarrow 2^1\text{S}$ transitions, for which, respectively, $\eta = 0.23$ and 0.65 are found, and the vacuum-ultraviolet resonant $n^1\text{P} \rightarrow 1^1\text{S}$ transitions, which exhibit strong self-absorption as indicated by η values being in the $10^{-5} - 10^{-4}$ range (at 1000 mTorr).

The comparison for the intensities, $I(x)$ of the 389 nm, 588 nm, and the 447 nm spectral lines is shown in figure 10. We find that except for the highest pressures, the shapes of the $I(x)$ curves and their relative amplitudes match fairly well between

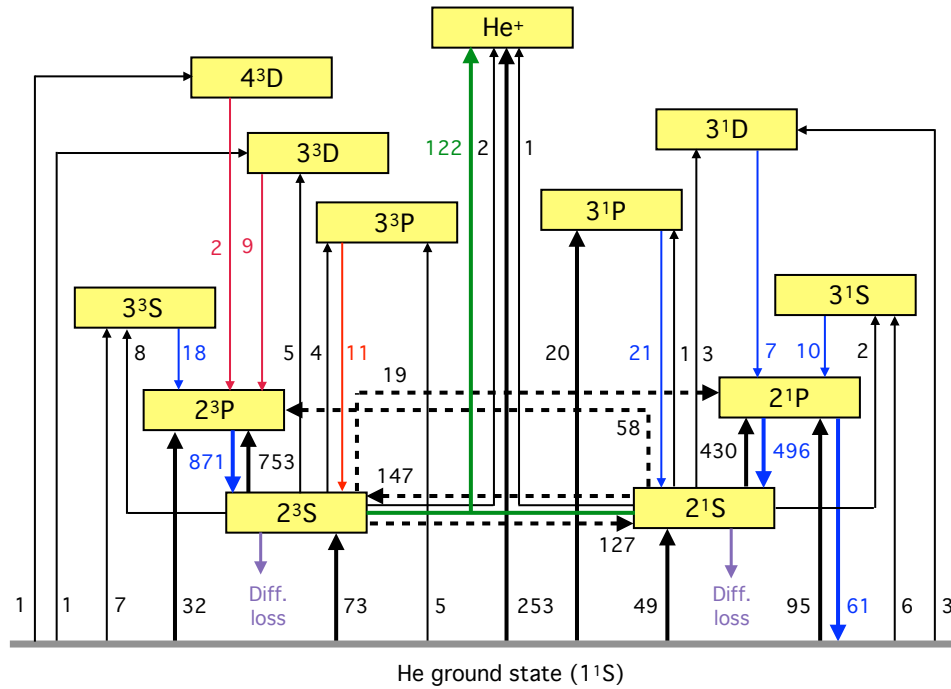


Figure 9. Same as figure 8, but for discharge conditions: $p = 1000$ mTorr, $V_{pp} = 350$ V, $L = 4$ cm.

experiment and simulation. At lower pressures both the experimental and the computational results show concave distributions peaking at the center of the plasma. With increasing pressure the distributions acquire a convex shape in the central bulk region. This transition is found to occur in the experiment between $p = 200$ mTorr and 500 mTorr, but is observed in the numerical result only at $p = 1000$ mTorr, representing a relatively major difference between the measured and computed distributions. The reason of this discrepancy requires further studies, however, it looks to be related to the density distributions of the excited atoms, as due to the weak self-absorption of the radiation on these transitions, the spatial distributions of the line intensities closely follow the shapes of the $n(x)$ density distributions of the excited atoms in the respective upper levels. These distributions are defined by the rates of the elementary processes, which ultimately depend on the cross sections and the EEDF.

A sensitivity analysis of the line intensity distributions on the elements of the cross section set is clearly beyond the scope of this work, however. Nonetheless, some insight can be gained based on the computational results. The change of the shape of the $I(x)$ curves is related to the dependence of the RF sheath width, s , and the electron energy relaxation length, λ_{en} , on the pressure. Actually, both quantities decrease when the pressure is increased. The sheath edge is the primary region where the electrons gain energy and the domain of the deposition of this energy is defined by λ_{en} . While at low pressures the electrons' motion is non-local (corresponding to high λ_{en}), at high pressures the energy gain and loss processes are more localized (small λ_{en}) and occur at

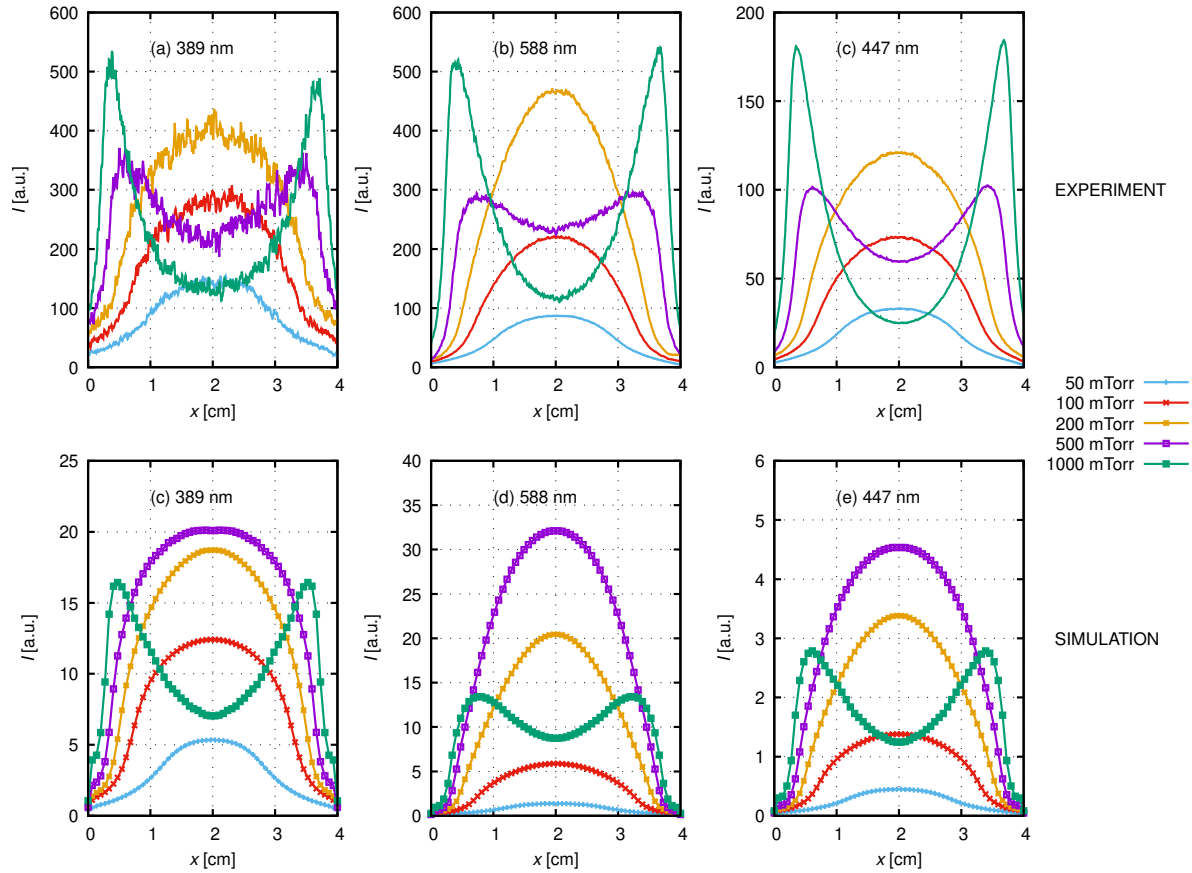


Figure 10. Comparison of the experimentally observed (top row) and computed (bottom row) intensity distributions for selected spectral lines (389 nm, 588 nm, and 447 nm, from left to right) at various pressures signified by the legend and $V_{pp} = 350$ V, $L = 4$ cm. The experimental intensities are corrected for the different acquisition times, transmissions, and detection efficiencies of the optical system at each wavelength to allow comparison to the computed intensity distributions.

the same domain of spatial positions. This is the reason why the direct electron-impact excitation rate, as discussed in relation to figure 6, has a broad maximum in the center of the gap at low p , but exhibits two marked peaks near the electrodes as the pressure is elevated. The intensities of the spectral lines of interest here, as discussed above, basically copy the densities of the excited atoms in the upper levels of these transitions. Since these densities are established by both direct electron-impact excitation (requiring high electron energy) and stepwise electron-impact excitation (efficient at low electron energy), it is the interplay of these processes that determines $I(x)$. Considering as an example the $3^3P \rightarrow 2^3S$ transition at 389 nm, we can see in figure 9 that the upper level is populated roughly equally from the 1^1S He ground state and the 2^3S metastable level. As the metastable atom density exhibits a relatively flat density distribution even at the highest pressure (see the density of 2^3S in figure 5), the transition with increasing p from concave to convex shape of $I(x)$ is partially hindered by the stepwise excitation process. This analysis suggests that the simulations somewhat overestimate the importance of the

stepwise reactions and/or the metastable densities. Clarification of the latter is planned via laser absorption measurements on the He 2^3S level population in the future.

5. Summary

LCIF measurements and 1d3v PIC/MCC simulations were performed in low-pressure capacitively-coupled radio-frequency discharges in helium gas. The studies are carried out for gas pressures between 50 mTorr and 1000 mTorr and peak-to-peak radio-frequency (13.56 MHz) voltages between 150 V and 350 V, applied to a highly symmetric source equipped with plane-parallel electrodes with separation distances of 4 cm and 2 cm. To determine n_e and (effective) T_e from the LCIF measurement data, analytical functions were developed and fit to data generated by a CRM for different gas pressures. Simulations were performed using a hybrid computational framework consisting of a PIC/MCC code and a Diffusion-Reaction-Radiation code that were executed iteratively. A good quantitative agreement was found between the experimental and simulation results for n_e and a reasonable agreement was found for T_e within the plasma bulk.

The simulation results provided further insights into the discharge operation. The density of the singlet 2^1S and triplet 2^3S metastables were similar at 100 mTorr, but at 1000 mTorr the singlet 2^1S metastables were significantly depleted. Pooling processes caused about 1/6 and 1/3 of the total ionization at 100 and 1000 mTorr, respectively, and stepwise ionization from the metastable levels was insignificant at both pressures. At 1000 mTorr, the coupling of the excited levels becomes stronger and there is significant stepwise excitation between the triplet/singlet $2S$ and $2P$ levels compared to 100 mTorr. A comparison to the intensity distributions of the 389 nm, 588 nm, and 447 nm spectral lines measured in the experiment suggested the simulations may somewhat overestimate the importance of the stepwise reactions and/or the metastable densities.

Acknowledgments

This work has been supported by the National Office for Research, Development and Innovation (NKFIH, Hungary) via grant K134462 and by Sandia National Laboratories' Plasma Research Facility, funded by the U.S. Department of Energy Office of Fusion Energy Sciences. Sandia is managed and operated by NTESS under DOE NNSA contract DE-NA0003525. AD was supported by the J. Bolyai Scholarship of the HAS. The authors would like to thank Dr. Ed Barnat at Sandia National Laboratories for helpful discussions. The authors would also like to thank Dr. Liam A. Padraic at Sandia National Laboratories for his help measuring the different transmissions and detection efficiencies of the optical system.

Disclosures

The authors have no conflicts of interest to disclose.

Data availability statement

The data that support the findings of this study are available within the article.

Appendix A. Analytic Functions for Recovering n_e and T_e from LCIF Measurements

The following analytic functions fit to data generated by a CRM are used to interpret the LCIF measurement data using corresponding coefficients in table A1. The CRM is the same as that of Barnat and Frederickson [36] and is applied with all the reactions and species they include.

$$x_1 = \log_{10}[\text{I}(588 \text{ nm})/\text{I}(389 \text{ nm})], \quad (\text{A.1})$$

$$x_2 = \log_{10}[\text{I}(477 \text{ nm})/\text{I}(588 \text{ nm})], \quad (\text{A.2})$$

$$\log_{10}(n_e) = 11.66 + 0.98x_1 + a_1 \exp(a_2x_1) + a_3 \exp(a_4x_1), \quad (\text{A.3})$$

$$T_e = p_{00} \quad (\text{A.4})$$

$$+ p_{10}x_1 + p_{01}x_2$$

$$+ p_{20}x_1^2 + p_{11}x_1x_2 + p_{02}x_2^2$$

$$+ p_{30}x_1^3 + p_{21}x_1^2x_2 + p_{12}x_1x_2^2 + p_{03}x_2^3$$

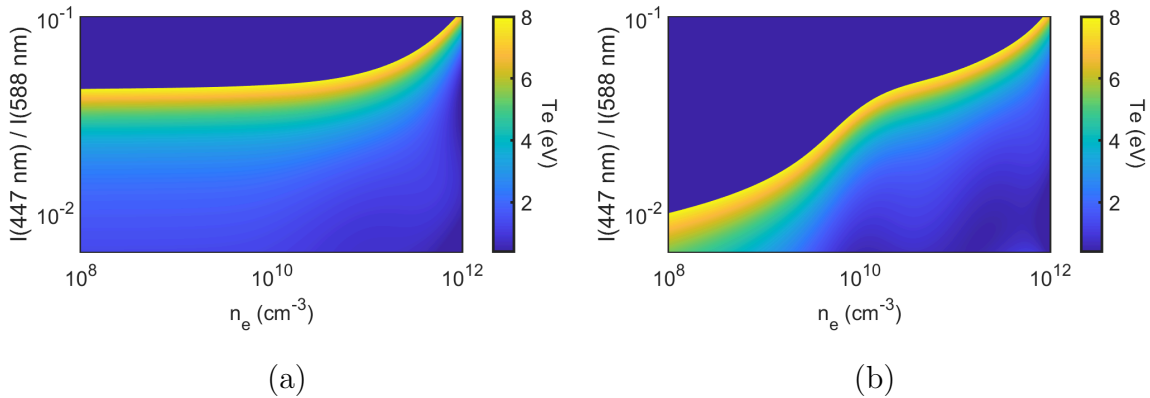
$$+ p_{40}x_1^4 + p_{31}x_1^3x_2 + p_{22}x_1^2x_2^2 + p_{13}x_1x_2^3 + p_{04}x_2^4$$

$$+ p_{50}x_1^5 + p_{41}x_1^4x_2 + p_{32}x_1^3x_2^2 + p_{23}x_1^2x_2^3 + p_{14}x_1x_2^4 + p_{05}x_2^5,$$

To generate the data required for fitting, at each pressure, the CRM is used to compute $\text{I}(588 \text{ nm})/\text{I}(389 \text{ nm})$ and $\text{I}(477 \text{ nm})/\text{I}(588 \text{ nm})$ for all combinations of 561 values of n_e between 10^8 and 10^{12} cm^{-3} and 761 values of T_e between 0.4 and 8 eV. Values significantly outside of these ranges are interpreted by the fitting functions and may be erroneous. The CRM is run a total of 2,561,526 times, and the computational time is about 12 hours on 600 cores. The fits are then determined using the robust linear least-squares fitting method in MATLAB. This routine performs an iterative search that finds the fitting coefficients by minimizing the difference between the set of n_e and T_e used as input to the CRM and the corresponding n_e and T_e predicted by eqs. A.3 and A.4. The root mean squared error is less than 0.05 for each fit. The application of these analytic fits requires LCIF measurements similar to those described in Section 2 [53]. For example, time-integrated measurements should be made lasting 50 ns and starting 50 ns after the laser pulse. Equation A.3 is plotted in figure 1(b) and eq. A.4 is plotted in figure A1 as a function of n_e at (a) 50 mTorr and (b) 1000 mTorr.

Table A1. Fitting coefficients for different pressures.

	25 mTorr	50 mTorr	100 mTorr	200 mTorr	500 mTorr	1000 mTorr
a1	-5.759×10^{-5}	-4.165×10^{-5}	-0.0002615	-0.0005286	-0.001066	-0.002281
a2	-2.642	-3.027	-2.642	-2.651	-2.73	-2.646
a3	-1.332×10^{-19}	-2.778×10^{-18}	-1.623×10^{-16}	-6.686×10^{-15}	-4.434×10^{-13}	-1.284×10^{-11}
a4	-12.3	-12.29	-12.3	-12.3	-12.47	-12.34
p00	337.8	296.7	286.6	293.2	276	271.8
p10	-123.5	-94.46	-72.64	-75.27	-91.36	-108.6
p01	816.7	690.2	640.5	656	613.7	602.8
p20	-35.36	-33.76	-42.63	-53.29	-60.57	-66.89
p11	-193.1	-127.3	-62.73	-52.08	-80.78	-112.3
p02	795.5	640.8	554.1	561.7	522	512
p30	-6.878	-7.315	-8.204	-7.301	-5.589	-5.576
p21	-36.2	-33.26	-48.39	-71.77	-93.05	-110.4
p12	-118.4	-63.09	5.356	33.36	21.59	4.89
p03	389.1	295.2	225.4	219.8	202	198.2
p40	-0.05237	-0.08007	-0.06096	0.3715	0.7186	0.3428
p31	-7.165	-7.672	-8.946	-9.368	-8.748	-8.658
p22	-8.964	-6.992	-14.9	-29.29	-44.6	-57.44
p13	-35.37	-15.04	15.63	34.31	36.23	34.83
p04	95.69	67.48	41.03	35.31	31.4	30.93
p50	-0.09945	-0.22	-0.4076	-0.7062	-1.558	-2.96
p41	0.2936	0.6357	1.101	1.903	3.44	5.149
p32	-2.191	-2.688	-3.45	-4.213	-4.872	-5.423
p23	0.2546	0.8282	-0.3728	-3.024	-6.293	-9.215
p14	-4.516	-1.784	3.15	6.979	8.317	8.957
p05	9.495	6.144	2.325	1.058	0.7055	0.7156

**Figure A1.** Helium LCIF. Calibrations derived using the CRM [36] that are used to determine T_e from the measurement data at (a) 50 mTorr and (b) 1000 mTorr.

References

- [1] Chabert P and Braithwaite N 2011 *Physics of Radio-Frequency Plasmas* (New York: Cambridge University Press)
- [2] Lieberman M A and Lichtenberg A J 2005 *Principles of Plasma Discharges and Materials*

- Processing, 2nd Edition* (Wiley)
- [3] Makabe T and Petrović Z 2006 *Plasma Electronics: Applications in Microelectronic Device Fabrication* London
 - [4] Derzsi A, Hartmann P, Vass M, Horváth B, Gyulai M, Korolov I, Schulze J and Donkó Z 2022 *Plasma Sources Science and Technology* **31** 085009
 - [5] Schulze C, Donkó Z and Benedikt J 2022 *Plasma Sources Science and Technology* **31** 105017
 - [6] Donkó Z, Hartmann P, Korolov I, Schulenberg D, Rohr S, Rauf S and Schulze J 2023 *Plasma Sources Science and Technology* **32** 065002
 - [7] Godyak V and Alexandrovich B 2015 *Journal of Applied Physics* **118** 233302
 - [8] Piejak R, Al-Kuzee J and Braithwaite N S J 2005 *Plasma Sources Science and Technology* **14** 734
 - [9] Yeom H, Kim J, Choi D, Choi E, Yoon M, Seong D, You S J and Lee H C 2020 *Plasma Sources Science and Technology* **29** 035016
 - [10] Lapke M, Oberrath J, Schulz C, Storch R, Styrnoll T, Zietz C, Awakowicz P, Brinkmann R P, Musch T, Mussenbrock T *et al.* 2011 *Plasma Sources Science and Technology* **20** 042001
 - [11] Peterson D, Ford K, Brandon J, Shannon S, Koh T, Chua T, Bera K, Tian W, Rauf S and Kraus P 2020 *Journal of Physics D: Applied Physics* **53** 145203
 - [12] Bienholz S, Styrnoll T and Awakowicz P 2014 *Journal of Physics D: Applied Physics* **47** 065201
 - [13] Schulz-von Der Gathen V, Röpcke J, Gans T, Käning M, Lukas C and Döbele H 2001 *Plasma Sources Science and Technology* **10** 530
 - [14] Engeln R, Klarenaar B and Guaitella O 2020 *Plasma Sources Science and Technology* **29** 063001
 - [15] Weßeling H J and Kronast B 1996 *Journal of Physics D: Applied Physics* **29** 1035
 - [16] Dzierżega K, Benck E, Roberts J *et al.* 1996 *Journal of Applied Physics* **80** 3196–3201
 - [17] Walsten A T, Bentz B Z, Youngman K and Xu K G 2024 *Physics of Plasmas* **31**
 - [18] Mansour ElSabbagh M, Bowden M, Uchino K and Muraoka K 2001 *Applied Physics Letters* **78** 3187–3189
 - [19] Weatherford B, Barnat E and Foster J 2012 *Plasma Sources Science and Technology* **21** 055030
 - [20] Surendra M and Graves D B 1991 *IEEE Transactions on Plasma Science* **19** 144–157
 - [21] Surendra M and Graves D 1991 *Applied Physics Letters* **59** 2091–2093
 - [22] Surendra M and Vender D 1994 *Applied physics letters* **65** 153–155
 - [23] Liang Y S, Li P B, Zhang Y R and Wang Y N 2024 *Journal of Physics D: Applied Physics* **58** 085205
 - [24] Turner M M 2006 *Physics of Plasmas* **13** 033506
 - [25] Vass M, Palla P and Hartmann P 2022 *Plasma Sources Science and Technology* **31** 064001
 - [26] Zheng B, Fu Y, Wen D Q, Wang K, Schuelke T and Fan Q H 2020 *Journal of Physics D: Applied Physics* **53** 435201
 - [27] Wen D Q, Krek J, Gudmundsson J T, Kawamura E, Lieberman M A and Verboncoeur J P 2021 *Plasma Sources Science and Technology* **30** 105009
 - [28] Wen D Q, Krek J, Gudmundsson J T, Kawamura E, Lieberman M A and Verboncoeur J P 2022 *IEEE Transactions on Plasma Science* **50** 2548–2557
 - [29] Bogaerts A, Gijbels R and Vlcek J 1998 *Journal of applied physics* **84** 121–136
 - [30] Kano K, Suzuki M and Akatsuka H 2000 *Plasma Sources Science and Technology* **9** 314
 - [31] Schulze M, Yanguas-Gil A, Von Keudell A and Awakowicz P 2008 *Journal of Physics D: Applied Physics* **41** 065206
 - [32] Akatsuka H 2019 *Advances in Physics: X* **4** 1592707
 - [33] Chai K B and Kwon D H 2021 *Spectrochimica Acta Part B: Atomic Spectroscopy* **183** 106269
 - [34] Horváth B, Derzsi A, Schulze J, Korolov I, Hartmann P and Donkó Z 2020 *Plasma Sources Sci. Technol.* **29** 055002
 - [35] Schulenberg D A, Korolov I, Donkó Z, Derzsi A and Schulze J 2021 *Plasma Sources Science and Technology* **30** 105003
 - [36] Barnat E and Frederickson K 2010 *Plasma Sources Science and Technology* **19** 055015
 - [37] Biagi magboltz 8.9 database www.lxcat.net accessed: January 13, 2024

- [38] Ralchenko Y, Janev R, Kato T, Fursa D, Bray I and De Heer F 2008 *Atomic Data and Nuclear Data Tables* **94** 603–622
- [39] Alves L, Gousset G and Ferreira C 1992 *Journal of Physics D: Applied Physics* **25** 1713
- [40] Phelps database www.lxcat.net/Phelps accessed: 7 Sept 2023
- [41] Drake G W and Morton D C 2007 *The Astrophysical Journal Supplement Series* **170** 251
- [42] Pitchford L C, Alves L L, Bartschat K, Biagi S F, Bordage M C, Bray I, Brion C E, Brunger M J, Campbell L, Chachereau A *et al.* 2017 *Plasma Processes and Polymers* **14** 1600098
- [43] Gangwar R, Sharma L, Srivastava R and Stauffer A 2012 *Journal of Applied Physics* **111** 053307
- [44] Kim H, Iza F, Yang S, Radmilović-Radjenović M and Lee J 2005 *Journal of Physics D: Applied Physics* **38** R283
- [45] Lymberopoulos D P and Economou D J 1995 *Journal of research of the National Institute of Standards and Technology* **100** 473
- [46] Donkó Z, Derzsi A, Vass M, Horváth B, Wilczek S, Hartmann B and Hartmann P 2021 *Plasma Sources Science and Technology* **30** 095017
- [47] Den Hartog E, Doughty D and Lawler J 1988 *Physical Review A* **38** 2471
- [48] Molnar J 1951 *Physical Review* **83** 940
- [49] Press W, Flannery B, Teukolsky S, Vetterling W and Chipperfield J 1987 Numerical recipes: the art of scientific computing
- [50] Capriotti E R 1965 *The Astrophysical Journal* **142** 1101
- [51] Bhatia A and Kastner S 2000 *Journal of Quantitative Spectroscopy and Radiative Transfer* **67** 55–63
- [52] Mewe R 1967 *British Journal of Applied Physics* **18** 107
- [53] White Z K, Gott R P, Bentz B Z and Xu K G 2023 *AIP Advances* **13** 085015